Radiation Enhancement in Plasmonic Bias-free and Antenna-less CW Terahertz Photomixer Emitters Array

Mohammad javad Mohammad-Zamani[1], Mohammad Kazem Moravvej-Farshi [1*], Mohammad Neshat[2]

Abstract:

We propose a new generation of unbiased (bias-free) antenna-less CW THz photomixer emitters array made of asymmetric MSM gratings with subwavelength pitch, operating in optical near-field regime. We take advantage of the size effects in near-field optics and electrostatics to demonstrate the possibility of enhancing the THz power by four orders of magnitude, as compared with a similar array of the same size that operates in the far-field regime. We show that with an appropriate choice of grating parameters in such THz sources the first plasmonic resonant cavity mode in nano-slit between two adjacent MSM can enhance the optical near-field absorption and hence the photo carriers' generation under the slit in the active medium. These photo carriers, on the other hand, are accelerated by the large built-in electric field sustained under the nano-slits by two dissimilar Schottky barriers to create the desired large THz power that is mainly radiated downward. A hybrid numerical simulation method is used to model and analyze these phenomena.

Keywords: Photomixer, Terahertz Emitters, Metal-Semiconductor-Metal, Plasmonics, Subwavelength structures

I. INTRODUCTION

Biased THz photomixers have shown to be potentially compact, low cost, low power consuming, coherent,

highly tunable, and room temperature CW THz sources [1, 2]. In this regard, the idea of using a bias free THz emitter can be a gateway to overcome the disadvantages appeared in the rival structures. A bias free THz photomixer is a potentially attractive THz radiation source for biomedical applications. As have already been demonstrated experimentally [3] and theoretically [4, 5], unlike the large aperture emitters [6], unbiased emitters with dis-similar Schottky contacts can efficiently accelerate photogenerated carriers. Moreover, unlike the scalable microstructured photoconductive emitters [7, 8], an unbiased antenna-free THz photomixer does not suffer from the likely occurring short circuiting defects in the gaps between adjacent fingers in interdigitated emitters that ruin the entire device operation. Above all, a bias free bimetallic THz emitter, unlike the unbiased lateral photo-Dember THz sources, does not suffer from the limitation in the choice of photoconductors with distinct electrons and holes mobilities [9, 10], relaxing the fabrication complexity. The most challenging issue that unbiased antenna-less MSM type photomixers with two dissimilar Schottky barriers are facing with could be their relatively low output THz power, as compared to the biased photomixers. Nonetheless, the total radiated power can be scaled up by the squared number of cells in the array in one dimension [5]. Employing a unit cell similar to that shown in Fig. 1, in that work, we have demonstrated that as the unit cell pitch (Λ) of the unbiased antenna-less THz photomixer emitters array, is reduced solely by reducing the slit (g) between two adjacent MSM strips the THz dipole radiation also decreases. Details of the unit cell constituents and its electrostatics are given in [5].

At the first glance, the aforementioned decrease in the THz output radiation power was not beyond anticipations. As a consequence of a decrease in g, the apertures through which the uncovered active medium can be irradiated are narrowed. And hence the amount of the absorbed light is reduced. Nevertheless, with a more clever insight one may also anticipate that with an appropriately designed slit of aspect ratio h/g, as g decreases below the subwavelength dimensions, Fabry-Perot like plasmonic cavity modes between the slit sidewalls could be excited. These plasmonic cavity modes enhance the optical transmission and consequently the absorption within the active regions under the nano-scaled (subwavelength) slits and hence increase the photogenerated carriers there. Meanwhile,

[1] Faculty of Electrical and Computer Engineering, Tarbiat Modares University, P O Box 14115-194, Tehran 1411713116, Iran
farshi_k@modares.ac.ir
[2]School of Electrical and Computer Engineering, University of Tehran, Tehran, Iran.

with a decrease in g the built-in field in the vicinity of the dissimilar Schottky contacts within the active medium, where the plasmonic assisted absorption enhances the photo carriers' generation also increases. These anticipations have motivated us to perform the current systematic analysis, exploiting the slit's size effects on the CW THz dipole power radiated out of the unbiased antenna-less MSM based photomixer emitters array.
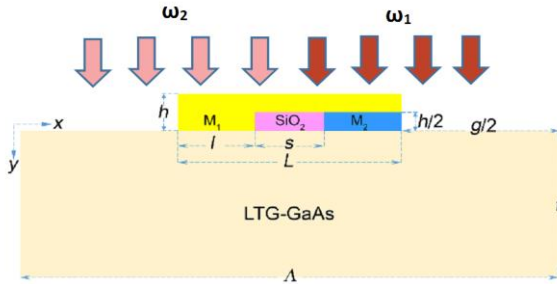

Fig. 1 x-y plane view of the unit cell of an unbiased antenna-less THz photomixer emitters array. Geometrical details are given in Table 1.

The rest of this paper is organized as follows. The proposed structure of the bias-free THz emitter together with its corresponding modeling and formulation used in numerical simulations of bias-free THz photomixer source are described in Section II. The numerical results and related discussions are given in Section III. Finally, the paper will be closed with conclusion.

II. DEVICES STRUCTURE, MODELING AND FORMULATION

As illustrated in Fig. 1, the unit cell of the unbiased antenna-less photomixer emitters array, under study, consist of an asymmetric MSM strip formed on top of a low temperature growth GaAs (LTG-GaAs) layer. The MSM is made of a pair of parallel but dissimilar metallic strips (M_1 and M_2) that make a pair of dissimilar Schottky barriers $\Phi_{B1} > \Phi_{B2}$, on LTG-GaAs. The lateral spacing between the two dissimilar contacts is filled by a SiO$_2$ stripe of width s. Permissible values of the pair of s and $\Delta\Phi_B = \Phi_1 - \Phi_2$, for which the maximum strengths of the built-in electric fields are below the critical value of 50 V/μm for breaking down the LTG-GaAs [11], are given in [5]. As also seen in Fig. 1, the metal strip with greater Schottky barrier (M_1) is extended over on top of the entire MSM to interconnect with M_2, providing the required current path within the unbiased MSM structure. The geometrical dimensions and the physical parameters related the materials constituting the unit cell are given in Table 1.

Table 1. Geometrical and physical parameters used in simulations.

Symbol	Parameter	Value	Unit
g	Slit (air-gap) lateral dimension	70-730	nm
h	Height of the slit side walls	22-810	nm
s	M$_1$-M$_2$ lateral spacing	70	nm
l	MS contacts lateral dimension	49-374.5	nm
$L = 2l + s$	MSM strip lateral dimension	168-819	nm
$\Lambda = L + g$	Pitch Size	240-900	nm
t	Substrate thickness	1	μm
λ_0	Laser center wavelength	800	nm
Δf	Input signals frequency difference	0.5	THz
I_0	Total optical power density	400	μW/μm^2
Φ_{B1}	Schottky Barrier height of M$_1$	1.11 [5]	eV
Φ_{B2}	Schottky Barrier height of M$_2$	0.91 [5]	eV
n_{b1}	Refractive Index of Metal 1	0.18+4.7i [21]	–
n_{b2}	Refractive Index of Metal 2	0.2+5i [21]	–

When two coherent CW optical signals of appropriate center wave-lengths with a frequency difference (Δf) in the desired THz band irradiate the un-covered LTG-GaAs surface through slits (air-gaps) separating the adjacent MSM strips, the absorbed light within the active region generates electron-hole pairs with a time-dependent generation rate, $G(x, y, t) = G(x, y) e^{j\omega t}$ with $\omega = 2\pi\Delta f$ being the modulation or beat note frequency. The built-in electric field, $E(x, y)$, accelerating the photogenerated electron-hole pairs is also modulated by the same frequency− i.e., $E(x, y, t) = E(x, y) e^{j\omega t}$. This triggers the radiation of the desired CW THz wave, in the absence of an external applied bias.

In order to model the bias-free THz photomixer, using the same procedure as reported in [12], initially we obtain the intensity distribution from the time-averaged optical Poynting vector to model the optical generation, using full wave simulations. In simulating the optical characteristics of the emitters, periodic boundary condition is applied at both unit cell boundaries, along the x-direction in the simulation domain. Moreover, employing the finite element method (FEM) in the time domain, the THz photocurrent inside the photoconductor is modeled. In this numerical simulation, drift-diffusion model including various generation mechanisms are considered, and appropriate boundary conditions for the Schottky metal-semiconductor interfaces and semiconductor-insulator interfaces along the outer boundaries are also applied. In the following, these steps are described in detail.

A. Optical Carrier Generation

Electron and hole pairs are generated by photon absorption when the gap is illuminated by two op

tical waves. For two plane wave excitations with difference of $\Delta\omega$, and a phase difference of φ, the intensity distribution is obtained from the time-averaged Poynting vector

$$S_{ave} = \frac{1}{2}\text{Re}(E \times H^*) \tag{1}$$

where E and H are the phasors of the optical electric and magnetic fields, respectively. The power density distribution, W, can be calculated as

$$W = -\nabla.S_{ave} \tag{2}$$

Then, the time-averaged optical generation rate, G_{opt}^{ave} is computed through the following equation:

$$G_{opt}^{ave} = \eta W / E_{ph} \tag{3}$$

Where E_{ph} is the photon energy and η is the quantum yield which gives the average number of charge carriers generated by a single photon. It should be noted that we calculate the time-averaged optical generation rate G_{opt}^{ave}, which is normally a constant number for typical cases where optical waves have the same frequency. In the present case, however, the optical frequencies are different, and therefore total optical generation rate is modulated by the difference frequency. This time-dependent optical generation rate should be considered in the set of drift–diffusion carrier transport equations which are to be numerically solved in the time domain. Therefore the total optical generation rate G_{opt}, becomes Error! Objects cannot be created from editing field codes. (4)

Employing the optical generation rate, the drift–diffusion partial differential equations can be solved by finite element method to achieve the generated THz photo-current inside the photoconductive layer of the photomixer.

B. Carrier Transport Model

The optical generation rate in (4) is now used in a carrier transport model to obtain the THz current and field around the active region in the photoconductor layer. There are various models to analyze charge carrier transport in semiconductor devices. In this paper, the drift–diffusion model is used to calculate the generated THz photo-current inside the photoconductor layer. The drift–diffusion mod-

average powers of P_1 and P_2, angular frequen el can explain physical phenomena such as optical generation of carriers and currents, and the field-screening effect. In addition, this model is sufficiently simple and therefore needs far less computational time as compared to other models [13]. A set of drift–diffusion equations in the time domain include the Poisson's equation, the continuity equations for electrons and holes, and the current relations for eletrons and holes as follows [14]

$$\nabla.(\varepsilon\nabla\phi(r,t)) = q\left(\text{N}_n(r,t) - \text{N}_p(r,t) - C_t(r,t)\right) \tag{5}$$

$$q\frac{\partial N_{n,p}(r,t)}{\partial t} = \pm\nabla.\vec{J}_{n,p}(r,t) + q\left[-R(r,t) + G(r,t)\right] \tag{6}$$

$$\vec{J}_{n,p}(r,t) = -q\mu_{n,p}N_{n,p}(r,t)\nabla\phi(r,t) \\ \pm qD_{n,p}\cdot\nabla N_{n,p}(r,t) \tag{7}$$

where ϕ is electrostatic potential, $N_{n,p}(r,t)$ are electron and hole densities, $\vec{J}_{n,p}(r,t)$ are electron and hole current densities, q is unit charge, ε is electrical permittivity, $C_t(r,t)$ is the concentration of additional, typically fixed, charges originated from charged impurities of donor (N_D) and acceptor (N_A) type, $R(r,t)$ is carrier recombination rate, $G(r,t)$ is carrier generation rate, $D_{n,p}(r,t)$ are electron and hole diffusion coefficients and $\mu_{n,p}(r,t)$ are electron and hole mobilities.

Substituting the current equations into the continuity equations from a set of the drift–diffusion equations, one can obtain three partial differential equations with the dependent variables of ϕ, N_n and N_p as follows [13]:

$$\nabla.(\varepsilon\nabla\phi(r,t)) = q\left(\text{N}_n(r,t) - \text{N}_p(r,t) - C_t(r,t)\right) \tag{8}$$

$$q\frac{\partial N_{n,p}(r,t)}{\partial t} = \nabla\cdot\left[D_{n,p}\nabla N_{n,p} - N_{n,p}\mu_{n,p}\nabla\phi\right] \\ -R(r,t) + G(r,t) \tag{9}$$

Equations (8) and (9) are solved self-consistently to obtain the electrostatic potential and carrier density in the photomixer device. The calculated quantities can then be used to characterize and analyze various parameters of the photomixer, such as the radiated THz power.

Note that when the cross-sectional dimension of the

device is comparable with the operating wavelength, Poisson's equation is not accurate enough for the electric field spatio–temporal behavior resulting from time-varying distributed charges. In that case, the wave equation should be used instead of Poisson's equation [13].

Carrier generation/recombination is an important process in optoelectronic devices. For the net recombination rate in the drift–diffusion model, the Shockley–Read–Hall (SRH) and Auger processes are considered.

The SRH process is caused by the absorption or emission of phonons. This process is trapping assisted, utilizing a lattice defect at the trap energy level within the semiconductor band gap. The net recombination rate R_{net}^{SRH} can be found by [14]

$$R_{net}^{SRH} = \frac{N_n N_p - n_i^2}{\tau_p (N_n + n_1) + \tau_n (N_p + p_1)} \qquad (10)$$

with

$$n_1 = n_i \exp\left(E_{trap}/kT\right) \qquad (11a)$$

and

$$p_1 = n_i \exp\left(-E_{trap}/kT\right) \qquad (11b)$$

Where n_i is the intrinsic carrier concentration, E_{trap} is the difference between the defect energy level and intrinsic energy level, and $\tau_{n.p}$ are the electron and hole carrier lifetimes.

Auger generation/recombination is typically important at high carrier densities. The direct band-to-band Auger process involves three particles. During generation, an electron-hole pair is created consuming the energy of a highly energetic particle. In recombination, when an electron-hole pair recombines, the resulting energy is transferred to another electron or hole.

The Auger net recombination rate can be obtained by [14]

$$R_{net}^{Auger} = (N_n C_n + N_p C_p)(N_n N_p - n_i^2) \qquad (12)$$

Where C_n and C_p are Auger capture coefficients for the electron and hole, respectively.

C. Boundary Conditions

For solving the set of drift–diffusion equations, appropriate boundary conditions should be considered. This section reviews the electrical boundary conditions which are considered in the modeling.

1) Metal–Semiconductor Interface (Schottky Contacts):

We adopt a model for Schottky contacts, which is based largely on the approach introduced by Crowell and Sze [15]. The semiconductor is assumed to be nondegenerate, since metal-degenerate semiconductor contacts are usually best represented by the ideal Ohmic option.

The contact acts as a source or sink for carriers and consequently it can be treated as a surface recombination mechanism:

$$\mathbf{J}_n \cdot \mathbf{n} = q v_n (n - n_0) \qquad (13a)$$

$$\mathbf{J}_p \cdot \mathbf{n} = q v_p (p - p_0) \qquad (13b)$$

Here, **n** is the outward unit vector normal to the surface of the semiconducting domain, v_n and v_p are the recombination velocities for electrons and holes, respectively, and n_0 and p_0 are the quasi-equilibrium carrier densities—that is, the carrier densities that would be obtained if it were possible to reach equilibrium at the contact without altering the local band structure. n_0 and p_0 are correspondingly defined as though the Fermi level of the semiconductor at the boundary is equal to that of the metal. n_0 and p_0 are given by:

$$n_0 = N_C \exp\left(-\frac{E_C - E_{fm}}{kT}\right) = N_C \exp\left(\frac{-\phi_B}{kT}\right) \qquad (14a)$$

$$p_0 = N_v \exp\left(-\frac{E_{fm} - E_v}{kT}\right) = N_v \exp\left(-\frac{E_g - \phi_B}{kT}\right) \qquad (14b)$$

Here, E_{fm} is the metal Fermi level, and ϕ_B is the emission barrier height for electrons (from the metal). From a practical perspective, in the proposed emitter the value of ϕ_B can be found from the results reported in the previous work for metal-LTG GaAs Schottky contacts [5].

2) Semiconductor–Insulator Interface:

At the interface between a semiconductor and an insulator, the boundary conditions are given by [14]

$$\varepsilon_{semi}\left.\frac{\partial\phi}{\partial n}\right|_{semi}-\varepsilon_{ins}\left.\frac{\partial\phi}{\partial n}\right|_{ins}=\rho_s \tag{15}$$

$$\mathbf{J}_n\cdot\mathbf{n}=-qR^{surf} \tag{16a}$$

$$\mathbf{J}_p\cdot\mathbf{n}=qR^{surf} \tag{16b}$$

Where ε_{semi} and ε_{ins} are the semiconductor and insulating material permittivity, respectively, ρ_s is the surface charge density at the interface, and R^{surf} is the surface recombination rate.

III. RESULTS AND DISCUSSIONS

Knowing the amplitudes of the optical generation rate and the built-in Schottky electric field, throughout the LTG-GaAs, we can evaluate the photomixer "efficiency" as define in [5,16].

$$\eta=\frac{\iint G\left(x,y\right)E\left(x,y\right)dxdy}{\max\left\{\iint G\left(x,y\right)E\left(x,y\right)dxdy\right\}}. \tag{17}$$

This efficiency is an indication of the generated power within the photomixer and can be used as a measure for optimizing the THz power.

By varying the unit cell geometrical parameters, g, *h*, and Λ, and employing FEM, we have calculated Eq. (17) for efficiency as a function of the pitch size and the slit aspect ratio— i.e., $\eta\left(\varLambda, h/g\right)$ — for a given slit to pitch ratio of $g/\varLambda=0.3$. The numerical results are illustrated in Fig. 2(a). Figures 2(b)-2(e) illustrate the distributions of magnetic field amplitude corresponding to points ($\varLambda$=490 nm, *h/g*=0.6), ($\varLambda$=250 nm, *h/g*=1.6), ($\varLambda$=590 nm, *h/g*=2.6), and ($\varLambda$=780 nm, *h/g*=1.6), as four examples whose significances will be discussed later. We have also calculated the efficiency as a function of the pitch size and slit to pitch ratio— i.e., $\eta\left(\varLambda, g/\varLambda\right)$ — for given $h/\varLambda=0.6$ and $h/\varLambda=0.3$. The numerical results are illustrated in Fig. 2(f) and Fig. 2(g), respectively. It is noteworthy that the values for the pair of *s* and $\Delta\varPhi_{\mathrm{B}}$, as given in Table 1, are chosen such that to enable us to vary g, *h*, and Λ over broad ranges also given Table 1, and yet having a great chance for the electric field to be less than the breakdown limit of 50 V/μm. The forbidden region, wherein the electric field exceeds the electrostatic breakdown limit, is within $\varLambda<240$ nm. The white area in Figs 2(f) and 2(g) also shows the forbidden region
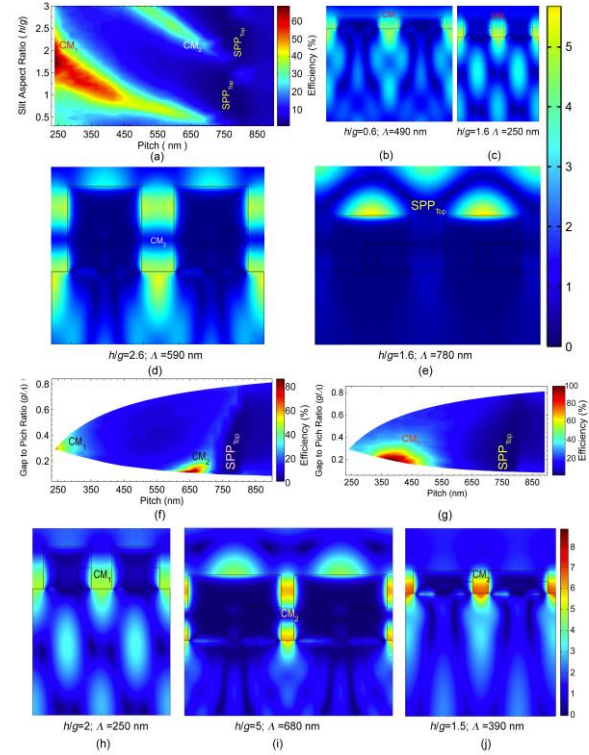

Fig. 2. (a) Distributions of η ($\varLambda$, *h/g*) for $g/\varLambda$= 0.3, (b)-(e) the magnetic fields amplitudes ($\left|H_Z\right|\times10^{-3}$) corresponding to CM$_1$ ($\varLambda$=490 nm, *h/g*=0.6), CM$_1$ ($\varLambda$=*250* nm, *h/g*=1.6), CM$_2$ ($\varLambda$=590 nm, *h/g*=2.6), and SPP$_{Top}$ ($\varLambda$=780 nm, *h/g*=1.6), (f) η ($\varLambda$, g /Λ) for $h/\varLambda=0.6$, and (g) η ($\varLambda$, g /Λ) for $h/\varLambda=0.3$, (h)-(j) the magnetic fields amplitudes ($\left|H_Z\right|\times10^{-3}$) corresponding to CM$_1$ (*h/Λ*=0.6, g /Λ=0.3, Λ=250), CM$_2$ (*h/Λ*=0.6 g /Λ=0.12, Λ=680), CM$_1$ (*h/Λ*=0.3 g /Λ=0.2, Λ=390)

As can be observed in Fig. 2(a), there are two isolated regions with considerable efficiencies (η>30%). These regions correspond to the first and second plasmonic mode resonances within the slits between each two adjacent MSM strips also known as "cavity modes (CMs)". As an example distributions of the magnetic fields amplitudes for CM$_1$ at two points ($\varLambda$=490 nm, *h/g*=0.6) and ($\varLambda$=*250* nm, *h/g*=1.6) are illustrated in Figs 2(b) and 2(c). The field distribution for CM$_2$ at point ($\varLambda$=590 nm, *h/g*=2.6) is also illustrated in Fig. 2(d). As also seen in Fig. 2(a) as the unit cell pitch approaches the incident wavelength, CM$_1$ and CM$_2$ both fade away. In other words plasmonic cavity mode resonances within the cavity appear for $\varLambda<\lambda_0$. This observation is similar to that reported in ref. [17, 18]. Also observed in this figure is a deep dark region (a valley in the efficiency color chart) that corresponds to the surface plasmon polariton resonances appearing on the top surface of the metal strip (SPP$_{Top}$), preventing the optical

19

power to penetrate into the active region. This is a phenomenon similar to that observed by [17, 19]. The magnetic field distribution showing SPP_{Top} for emitters with Λ=780 nm, g/Λ =0.3, and h/g=1.6 is illustrated in Fig. 2(e).

Also seen in Fig. 2(a) is that as the pitch size is decreased, for a constant g/Λ, the peak efficiencies for both cavity modes move toward the larger h values. This is attributed to the Fabry Perot relation $h = (2m-1)\lambda_{eff}/4$, wherein m and λ_{eff} are the mode number and effective wavelength, respectively. Moreover, in the same figure, one can also observe that as the pitch size decreases, the peak value in efficiency increases. This follows our earlier discussion in regard to the increase in the Schottky built-in field resulted from a decrease in g. Hence, the highest peak efficiency observed for emitters with pitches in the range of $\Lambda \sim$ 240-250 nm (g~72-75 nm) is a consequence of occurrence of the plasmonic enhanced photogeneration (by CM_1) within the region where the Schottky built-in field is approaching its highest permissible value.

As observed from Fig. 2(f), the two high efficiency regions corresponding to CM_1 and CM_2 both cover very narrow ranges of variations in Λ and the g/Λ. Moreover, the peak efficiency region in this figure occurs in a very narrow region with small g/Λ. This is similar to the discussion about the high η values that can be observed within $\Lambda \sim$ 240-250 nm. In this case also due to the small slit size the intense built-in Schottky field is multiplied by the photogenerated carrier density. Also, the similar behavior can be seen in Fig. 2(g) (with given h/Λ = 0.3). However, there is only one high efficiency region corresponding to CM1 covering the ranges of variations in Λ and the g/Λ.

As observed from Fig. 2(b)-Fig. 2(d) and Fig. 2(h)-Fig. 2(j) for arrays with $\Lambda < \lambda_0$, the near field plasmonic cavity modes confine the light intensity under the slits within the active region near the surface, where the lateral built-in electric field (E_x) is significant while its transverse (E_y) component is smaller [5]. Conversely, under the MSM strips, where $E_x < E_y$ [5], the light intensity and hence the photogeneration is infinitesimal. From these, we anticipate that the plasmonic cavity modes mainly enhance the lateral component of the THz dipoles current, increasing the THz radiation in transverse (y) direction. With this anticipation, we evaluate the effective dipole current densities for both lateral (J_{eff-x}) and transverse (J_{eff-y}) directions for a single pitch, using

finite element method (FEM). In doing so one needs to know the local THz photocurrent density [5],

$$\mathbf{J}_{ph}(x,y,t) = \mathbf{J}_{DC}(x,y) + \mathbf{J}_{AC}(x,y)\cos(\omega t), (18)$$

Where $J_{DC}(x,y)$ and $J_{AC}(x,y)$ are the DC component and the amplitude of the AC component of the local photocurrent density, respectively.

Since the wavelength of the THz radiation (λ_{THz}) is much longer than the dimensions of the photomixer, under study, the lateral and transverse components of the local currents at all points inside the active region add-up coherently, resulting in the effective dipole current densities for both lateral and transverse directions:

$$J_{eff-x}(t) = J_{eff-x} e^{j\omega t} \qquad (19a)$$

$$J_{eff-y}(t) = J_{eff-y} e^{j(\omega t - \varphi)} \qquad (19b)$$

Where φ represents the phase difference between the two effective components.

Figure 3(a)-3(c) illustrate the numerical results obtained for the amplitudes of J_{eff-x} and J_{eff-y} versus Λ for g/Λ=0.3, corresponding to three values for h/g= 0.6, 1.6, and 2.6, respectively, taken from Fig. 2(a). Figure 3(a), showing the current enhancement by CM_1 about Λ=490 nm corresponds to Fig. 2(b). Figure 3(b) that is related to Fig. 2(c), represents the current enhancement by CM_1 about Λ=250 nm. Figure 3(c) that corresponds to Fig. 2(d), is showing the current enhancement by CM_2 about Λ=590 nm. Figures 3(d)-3(f) illustrate the time dependence of the lateral and transverse effective current densities per pitch in arrays with corresponding to the peak values illustrated in Figs. 3(a)-3(c), respectively. These results show that the current enhancement in the emitters array with smallest possible pitch and the given slit aspect ratio is stronger than the other two arrays. This is certainly due to the enhancement of photocarrier generation by the plasmonic cavity modes of nano-slits within the region that the built-in Schottky electric field attains it maximum permissible strength.

The magnitude of the dipole current density is an indication of the THz output power. Moreover, for the emitters under study, by adding of all elementary Hertzian dipole emissions at various points inside the active region coherently one can obtain the total THz power. Hence, we can easily neglect any spatial phase shifts. In other words THz radiated power of a single pitch can be estimated by [5, 20]:

20

Error! Objects cannot be created from editing field codes.   (20)
where

$$R_{\text{rad}} = \frac{2\pi Z_0 \sqrt{\varepsilon_{\text{eff}}}}{3} \left[\frac{l_0}{\lambda_{\text{THz},0}} \right]^2 \text{ with } l_0 = v_{\text{sat}}\tau_{\text{rec}} \quad (21)$$

Is the radiation resistance. Parameter Z_0 and ε_{eff} are the free space impedance and the air/semiconductor interface effective relative permittivity, respectively, and l_0 $(=v_{\text{sat}}\tau_{\text{rad}})$ represents the dipole effective length with v_{sat} and τ_{rec} representing the carriers' saturation velocity and recombination lifetime, respectively.

The radiation mechanism in the proposed photomixer is similar to that of biased large area emitters such as large aperture emitters [6] and the scalable microstructured THz emitters [7, 8]. The acceleration and separation of photocarriers induce a time-varying dipole moment within the active region that generates terahertz radiation. For this antenna-less concept, a collection of Hertzian electron and hole dipoles generated by the photomixer, themselves, act as the antenna.

By using Eqs. (20) and (21), we have estimated the THz power radiated from emitters of Fig 3 by considering an active area of 70 μm^2 ($7\mu m(Length) \times 10\mu m(\text{width})$) for the each of them, as illustrated in Fig. 4.
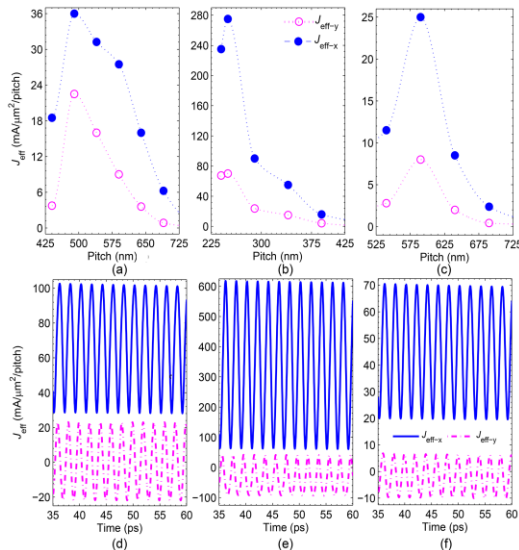

Fig. 3. (a)-(c) Amplitudes Jeff-x and Jeff-y versus Λ for h/g = 0.6, 1.6, and 2.6; and (d)-(f) time dependencies of the effective current components for emitters with (Λ, h/g) = (490 nm, 0.6), (250 nm, 1.6), and (590 nm, 2.6).
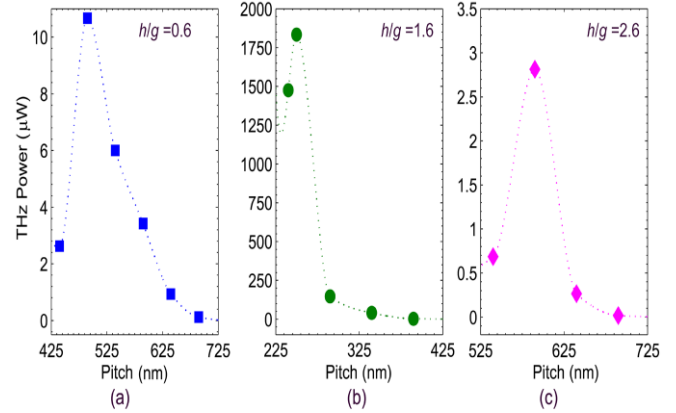

Fig. 4. (a)-(c) THz power radiated out of the emitters of Figs. 3(a)-(c), respectively. All the emitters have an active area of 70 μm^2.

As we have discussed earlier, in this paper, the THz power radiation is mostly directed downward, because in addition to $J_{\text{eff-x}} > J_{\text{eff-y}}$ the substrate impedance is less than that of the free space.

Comparison of the results depicted in Fig. 4 with a similar graph reported by [5] for the same active area (70 μm^2 used for here) reveals that by taking advantage of the near-field plasmonic cavity modes to enhance the optical absorption and hence the carriers photogeneration within the active region of the proposed device the maximum obtainable power in the worst case (see Fig. 4(c)) is about 30 times greater than that can be obtained by the emitters in which the absorption is diffraction limited (see Fig. 13(a) of [5]). It is worth noting that this enhancement was achieved mainly by the second cavity mode within slits of h~0.58 λ_0, and g ~0.22 λ_0 on an array of pitch Λ~0.74λ_0. Also seen in this figure, as the emitters pitch reduces to Λ~0.61 λ_0 and the cavity dimensions also become h~0.12 λ_0, and g ~0.18 λ_0 the first cavity mode takes the lead to enhance the absorption and carriers photogeneration (Fig. 4(a)), as a consequence of which the maximum obtainable THz power becomes even 3.8 times larger than that obtained by the help of the second cavity mode. Decreasing the emitters' pitch even further to Λ~0.31 λ_0 with nano-cavities of h~ 0.15 λ_0, and g ~0.09 λ_0, in addition to the enhancement of absorption and hence photogeneration, by the first cavity mode, the high built-in field amplifies the current and hence the radiation power (Fig. 4(b)). This is because the effective current is proportional to the photogenerated carriers' density and the electric field and the THz power is proportional to the square of the effective current.

As seen from Fig. 4(b), the highest permissible per pitch peak power obtained by the emitters with the smallest pitch (Λ=250 nm, g= 75 nm, and h=120 nm) operating in the optical near-field regime is about 680 times larger than that by the similar emitters operating in diffraction limited (far-field) regime with a 5.6 times larger pitch, as reported by [5]. In other words, the total radiated THz power from a chip consisting an array of (N_{NF}×1) near-field emitters like those of Fig. 2(c) is about 2×10^4 times larger than the total power radiated from another chip of the same area that contains an array of (N_{FF}×1) far-field emitters of ref [5]. This is because, the total power is scaled up by square of N_{NF} and N_{FF} that represent the number of pitches in the single row of near- and far-field operating arrays, respectively. Nevertheless, such power ratios for similar arrays made of near-field emitters like those of Figs. 2(b) and 2(d), reduce in proportion. It is apparent that if the number of rows in each array also increases, the absolute radiated THz power of that array increases by the square of the same number. Hence, an appropriately chosen array with a certain numbers of rows and columns with any of the three near-field emitters of Figs 2(b)-2(d) may provide the required THz output power as desired for a specific application. These large area unbiased emitters can offer high-power terahertz radiation because of their capacity to handle relatively high optical powers without suffering from the carrier screening effect and thermal breakdown.

IV. CONCLUSION

In conclusion, we have designed a new generation of unbiased antenna-less CW THz photomixers arrays, operating in optical near-field regime. We have taken advantage of the size effects to enhance the carriers' photogeneration within the active region and increase the built-in electric field induced by two dissimilar Schottky barriers in the same region. As a consequence of these two enhancements that multiply each other, maximum obtainable power radiated from a near-field operating THz chip is increased by more than four orders of magnitudes as compared with the power radiated from a similar far-field operating THz chip of the same size. Such THz sources can pave the way to various biomedical applications like endoscopic imaging without a need for hazardous external circuitry for biasing, reducing the patient health risk.

REFERENCES

[1] I. S. Gregory, C. Baker, W. R. Tribe, I. V. Bradley, M. J. Evans, E. H. Linfield, A. G. Davies, and M. Missous, "Optimization of photomixers and antennas for continuous-wave THz emission," IEEE J. Quantum Electron. 41(5), 717-728 (2005).

[2] M. C. Teich, "Field-theoretical treatment of photomixing," Appl. Phys. Lett. 14(6), 201–203 (1969).

[3] M. Nagel, "Photoconductive structure e.g. radiation source, for optical generation of field signals in terahertz-frequency range in bio analysis, has metallic layers formed from locations and provided in direct contact with semiconductor material , European Patents Office, 2013, DE102012010926 (A1)

[4] M. J. Mohammad-Zamani, M.K. Moravvej-Farshi, and M. Neshat, "Modeling and designing an unbiased CW terahertz photomixer emitters," Millimeter-Wave and Terahertz Technologies (MMWATT), 2014 Third Conference on, http://dx.doi.org/10.1109/MMWaTT. 2014.7057196.

[5] M. J. Mohammad-Zamani, M.K. Moravvej-Farshi, and M. Neshat, "Unbiased CW terahertz photomixer emitters with dis-similar Schottky barriers," *Opt. Express*. 23(15), 19129-19141, 2015.

[6] J. T. Darrow, X.-C. Zhang, D. H. Auston, and J. D. Morse, "Saturation Properties of Large-Aperture Photoconducting Antennas," IEEE J. Quantum Electron. 28(6), 1607-1616 (1992).

[7] S. Winnerl, "Scalable microstructured photoconductive terahertz emitters," J. Infrared Milli. Terahz. Waves 33, 431-454 (2012).

[8] A. Dreyhaupt, S. Winnerl, T. Dekorsy and M. Helm, "High-intensity terahertz radiation from a microstructured large-area photoconductor," Appl. Phys. Lett. 86, 121114 (2005).

[9] G. Klatt, F. Hilser, W. Qiao, M. Beck, R. Gebs, A. Bartels, K. Huska, U. Lemmer, G. Bastian, M.B. Johnston, M. Fischer, J. Faist, and T. Dekorsy, "Terahertz emission from lateral photo-Dember currents," Optics Express 18(5), 4939-4947 (2010).

[10] V. Apostolopoulos and M. E. Barnes,"THz emitters based on the photo-Dember effect*,"* J. Phys. D: Appl. Phys. 47, 374002 (2014).

[11] E. R. Brown, "THz generation by photomixing in ultrafast photoconductors," Int. J. High Speed Electron. Syst. 13(2), 497-545 (2003).

[12] M. Khabiri, M. Neshat and S. Safavi-Naeini, "Hybrid Computational Simulation and Study of Continuous Wave Terahertz Photomixers," IEEE Tran. Terahz. Sci. Technol. 2(6), 605-616 (2012).

[13] M. Neshat, D. Saeedkia, L. Rezaee and S. Safavi-Naeini, "A Global Approach for Modeling and Analysis of Edge-Coupled Traveling-Wave Terahertz Photoconductive Sources," IEEE Transactions on Microwave Theory & Techniques, vol. 58, no. 7, pp. 1952 - 1966, July 2010.

[14] S. Selberherr, Analysis and Simulation of Semiconductor Devices. Wien, Austria: Springer-Verlag, 1984.

[15] C. R. Crowell and S. M. Sze, "Current Transport in Metal-Semiconductor Barriers," Solid State Electronics, vol. 9, pp. 1035 1048, 1966

[16] S. Jafarlou, M. Neshat and S. Safavi-Naeini, "A Hybrid Analysis Method for Plasmonic Enhanced Terahertz Photomixer Sources," Optics Express, Vol. 21, No. 9, pp. 11115-11124, April 2013.

[17] Porto, J. A., F. J. Garcia-Vidal, and J. B. Pendry. "Transmission resonances on metallic gratings with very narrow slits." *Physical review letters* 83.14 (1999): 2845.

[18] B.-Y. Hsieh and M. Jarrahi, "Analysis of periodic metallic nano-slits for efficient interaction of terahertz and optical waves at nano-scale dimensions," *J. Appl. Phys*. 109, 084326, 2011

[19] P. Zilio, D. Sammito, G. Zacco, and F. Romanato, "Absorption profile modulation by means of 1D digital plasmonic gratings," Opt. Express. 18, 19558–19565 (2010).

[20] S. Preu, G. H. Döhler, S. Malzer, L. J. Wang, and A. C. Gossard , "Tunable, continuous-wave Terahertz photomixer sources and applications," J. Appl. Phys. 109, 061301-56 (2011).

[21] E. D. Palik, Handbook of Optical Constants of Solids (Academic, 1998).

23